J Mater Sci (2017) 52:13886–13896

Electronic materials

Nanocrystalline copper sulfide and copper selenide thin films with p-type metallic behavior

C. Guillén[1,*] and J. Herrero[1]

[1] *Department of Energía, CIEMAT, Avda. Complutense 40, 28040 Madrid, Spain*

Received: 27 June 2017
Accepted: 18 August 2017

ABSTRACT

Copper chalcogenide materials are interesting for multiple applications due to the feasibility of suiting their optical absorption and electrical conduction by the creation of copper vacancies. Here, Cu_xS and Cu_xSe nanocrystalline films with p-type conductivity have been obtained by heating evaporated copper layers of various thicknesses with elemental sulfur or selenium, at temperatures ranging from 250 to 400 °C. These preparation parameters determine the composition and the crystalline structure of the samples, which in turn control their morphology, optical and electrical properties. Thus, the surface roughness increases with the mean crystallite size, whereas the hole concentration increases as the copper atomic proportion (or x value) decreases. Owing to the high carrier densities achieved, around 10^{22} cm^{-3}, the samples show a metallic behavior with plasmonic absorption in the near infrared and electrical transport dominated by phonon scattering. Apart from such common behavior, some differences have been established between the sulfide and selenide films. One is the superior thermal stability of hexagonal CuS, present in all the temperature range, with respect to hexagonal CuSe, which evolves to cubic $Cu_{1.8}Se$ above 300 °C. Other is about the bandgap, wider for the sulfide than selenide samples.

Introduction

Binary copper sulfides and selenides synthesized as nanoparticles or thin films are attracting a growing interest due to their unique properties and multiple applications in catalysis, sensors, batteries, solar control glazing and photovoltaic devices [1–6]. They exhibit different stoichiometry and crystal structures [7, 8] that determine their optical and electrical properties. The gap energy of cubic Cu_2S and Cu_2Se, 1.0–1.3 eV in bulk materials [9, 10], is suitable for light absorption under sunlight illumination [11]. Nevertheless, the bandgap shows a high sensibility to structural distortions and stoichiometric variations, which are favored by the mobility of Cu ions and the thermodynamic propensity toward Cu deficiency, together with the ability of Cu and chalcogen (S or Se) to change their oxidation state [9, 12, 13]. In fact, these compounds are denoted as Cu_xS or Cu_xSe (generally with $1 \leq x \leq 2$), where a lower x value represents a higher Cu deficiency. The copper vacancies act as electron acceptors and make them p-type semiconductors, which achieve metallic

---

Address correspondence to E-mail: c.guillen@ciemat.es

DOI 10.1007/s10853-017-1489-4

character when the hole density overcomes 10^{21} cm^{-3} [14, 15]. Such copper deficiency can produce some gap widening by reduced Cu d-band width, in addition to the Moss–Burstein widening by increased carrier concentration [12, 16]. But this is counterbalanced by many-body effects that tend to shrink the bandgap, due to the contribution of scattering to the self-energy of the carriers [16, 17].

The facility for intrinsic doping is of especial interest in the production of Cu_xS and Cu_xSe for plasmonic applications, where the possibility to switch the resonance frequency by changing the composition and geometry of nanocrystallites has a great relevance [18–21]. In bulk materials, the plasmon frequency can be moved from the infrared toward the visible range by increasing doping [22]. Otherwise, when the plasmon oscillations are confined to nanoparticles, the resonance frequency changes also with their size and shape [23]. Thus, nanoparticles of noble metals are often chosen for n-type plasmon generation in the visible and near infrared, but highly doped semiconductors can produce analogous response and exceptionally they allow for controlled n-type or p-type conductivity as required [16, 23]. For nanocrystalline thin films, the crystallite size and other properties are also modified with the layer thickness [24–26]. Moreover, highly doped semiconductors offer a good chance for exploring the relationship between the charge carrier properties and the plasmonic response, owing to the lack of multiple transitions that complicate the spectral response in metals [27, 28].

In the present work, Cu_xS and Cu_xSe nanocrystalline films have been obtained by heating evaporated copper layers of various thicknesses with elemental sulfur or selenium, at temperatures ranging from 250 to 400 °C. Thermal annealing of copper in reactive atmospheres has been performed in different ways [29, 30]. The experimental procedure here is analogous to that used in the preparation of chalcopyrite compounds for photovoltaic applications [31, 32]. The availability of sulfur or selenium in excess has been ensured to achieve p-type intrinsic doping through the formation of copper vacancies. The influence of the annealing temperature and copper thickness on the crystalline structure, morphology, optical and electrical properties of the samples has been determined and analyzed comparatively for copper sulfide and copper selenide films. Plasmonic characteristics connecting the electrical and optical properties have been established for these materials, as well as their dependence on the preparation parameters.

Experimental details

First, copper thin films were deposited by e-beam evaporation of Cu pellets (99.99% purity) on soda lime glass substrates placed in a rotating holder. The pressure during evaporation was maintained below 4×10^{-6} mbar. The growth rate was fixed at 0.2 nm/s, and the film thickness was changed from 50 to 200 nm by increasing the deposition time, being always controlled through quartz crystal monitoring. Subsequently, the evaporated Cu layers were annealed with elemental sulfur or selenium pellets put together in a partially closed graphite container, which was loaded into a quartz tube furnace. Chalcogen (S or Se)-to-copper mass ratio was adjusted according to previous studies [33]. The reaction processes were carried out under flowing Ar (0.5 l/min) and atmospheric pressure, at different annealing temperatures from 250 to 400 °C that were maintained during 30 min.

For the various copper sulfide and copper selenide samples, the atomic composition was determined with a Fischer X-ray fluorescence analyzer using tungsten anode. The structure was examined by X-ray diffraction (XRD) with radiation Cu $K\alpha_1$ ($\lambda = 1.54056$ Å) in a Philips X'pert instrument. Crystallographic phases have been identified by comparison of the measured diffraction peaks with the cards given by the Joint Committee of Powder Diffraction Standards (JCPDS). For each phase, the mean crystallite size has been estimated with the Scherrer formula from the full-width at half-maximum of the main diffraction peak. The morphology was characterized with a Park XE-100 atomic-force microscope (AFM), by taking digital images that allow quantification of the surface roughness. Optical transmittance T and reflectance R measurements were taken with unpolarized light at normal incidence in the wavelength range 300–2400 nm, with a double beam spectrophotometer PerkinElmer Lambda 9, taking the air as reference. The absorption coefficient has been calculated as $\alpha = (1/t)\ln\{(100 - R(\%))/T(\%)\}$, including also the film thickness value (t) that was determined by profilometry with a Dektak 3030. Electrical conductivity, free charge carrier concentration and mobility were obtained with an ECOPIA system based on Hall effect measurements.

Results and discussion

The composition of the samples is found dependent on the initial copper thickness in addition to the heating temperature applied for sulfurization or selenization, as it is represented in Fig. 1. This shows that the copper-to-chalcogen atomic ratio is near to unity for the thinnest films heated at relatively low temperature (250–300 °C). The copper proportion increases when the annealing temperature rises to 350 °C, achieving a maximum value that is higher for the selenized layers (Cu/Se = 2.2) than for the sulfurized samples (Cu/S = 1.2). Otherwise, for a same reaction temperature the copper proportion decreases when the film thickness increases, being the minimum value achieved in the low-temperature range similar after selenization (Cu/Se = 0.6) and sulfurization (Cu/S = 0.7). The dependence with the thickness has been confirmed by simultaneous reaction of various Cu layers in a same process. All these compositional data should be analyzed in relation to the respective crystalline structure, which is detailed below.

The influence of the copper thickness on the crystalline structure of sulfurized and selenized samples is evidenced by the XRD patterns depicted in Fig. 2, corresponding to 250 °C heating temperature. The thinnest films show crystallization of hexagonal CuS (JCPDS no. 06–0464) or CuSe (JCPDS no. 06–0427) with strong (006) orientation. Thus, hexagonal crystallites tend to grow with *c* axis perpendicular to the substrate, in the same way than observed for these compounds prepared by electrodeposition [3] or pulsed laser ablation [34], but the increment in the film thickness promotes also different crystalline orientations. Such more random growth is related to a higher chalcogen (S or Se) incorporation that produces crystallization of orthorhombic $CuSe_2$ (JCPDS no. 19–0400) for the thickest selenized layer, according to its compositional data (Cu/Se = 0.6), although only hexagonal CuS is detected for the analogous sulfurized sample.

The evolution of the crystalline structure with the heating temperature is illustrated in Fig. 3. An

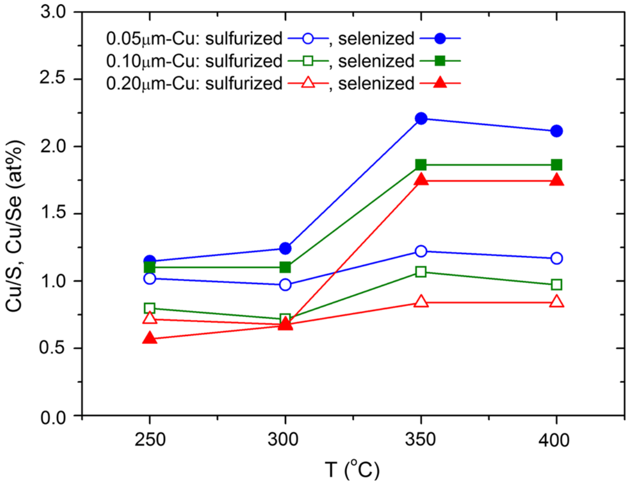

Figure 1 Evolution of the sample composition (Cu/S or Cu/Se atomic ratio) as a function of the reaction temperature and the evaporated Cu film thickness.

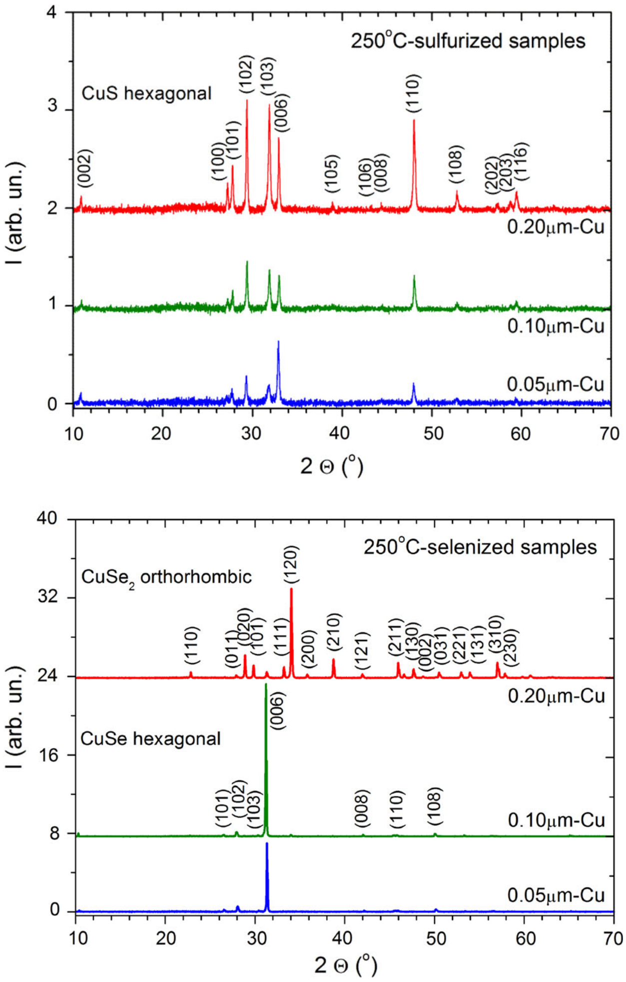

Figure 2 XRD patterns corresponding to various Cu film thicknesses after sulfurization or selenization at 250 °C.

additional cubic $Cu_{1.8}S$ phase (JCPDS no. 24–0061) is detected together to the hexagonal CuS for the layers sulfurized at 400 °C. This is due to some evolution from CuS to more stable $Cu_{1.8}S$, increasing the symmetry by heating [35], although the composition of these samples ($Cu/S \leq 1.2$) indicates that CuS remains in a high proportion, as observed in other works [7, 15]. Conversely, for the selenized films the increment in the reaction temperature to 350 °C produces a large compositional change ($Cu/Se \geq 1.7$) owing to the crystallization of cubic $Cu_{1.8}Se$ (JCPDS no. 06–0680) substituting the hexagonal CuSe, along with tetragonal Cu_3Se_2 (JCPDS no. 47–1745) for the thickest samples with an overall ratio $Cu/Se \sim 1.7$. These results confirm that thermal annealing involves phase transitions from hexagonal to cubic and tetragonal structures, by increasing the crystal symmetry and the Cu/Se ratio in the way [35]. The normalized cell volume per formula unit increases with such phase transformations owing to thermal expansion and Cu rearrangement processes as stated in the bulk materials [36, 37].

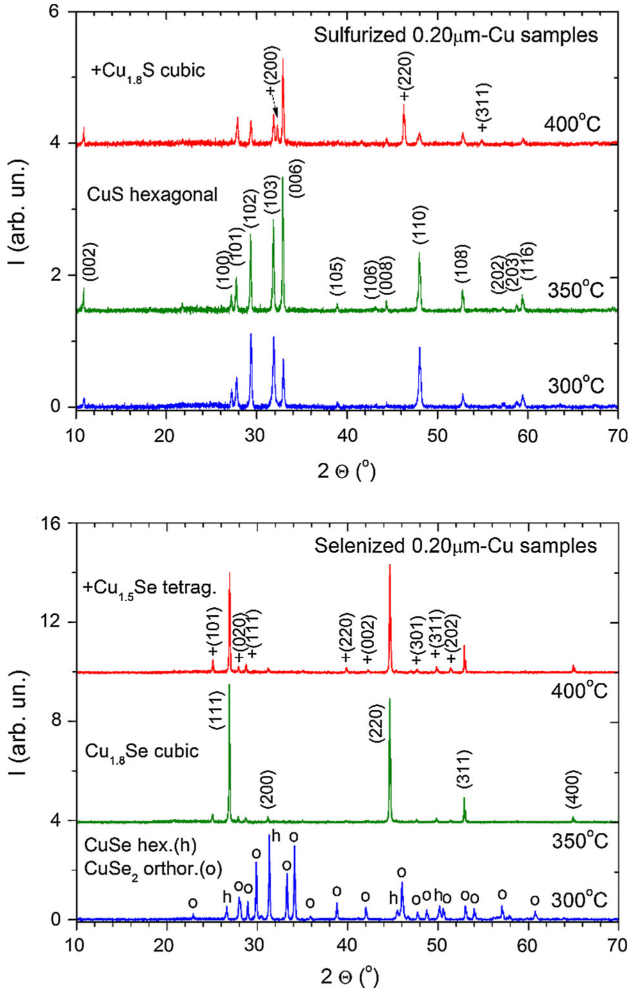

Figure 3 XRD patterns corresponding to 0.2-µm-thick Cu films after sulfurization or selenization at various temperatures.

The reactions involved in the formation of the various crystalline compounds should be related to the chalcogen species in the gas phase. Below 330 °C, the allotropes S_8 and Se_6 are the dominant species in sulfur and selenium gasses, respectively [38, 39]. Above 330 °C, S_2 becomes more relevant in the sulfur gas, whereas Se_5 and Se_2 are the favorable species in the selenium case [39]. Therefore, the following equilibria are considered for the compounds obtained at $T \leq 300$ °C:

$$8Cu(s) + S_8(g) \rightarrow 8CuS(s) \tag{1}$$

$$6Cu(s) + Se_6(g) \rightarrow 6CuSe(s) \tag{2}$$

$$3Cu(s) + Se_6(g) \rightarrow 3CuSe_2(s) \tag{3}$$

and for $T \geq 350$ °C:

$$2Cu(s) + S_2(g) \rightarrow 2CuS(s) \tag{4}$$

$$9Cu(s) + Se_5(g) \rightarrow Cu_9Se_5(s) \tag{5}$$

$$3Cu(s) + Se_2(g) \rightarrow Cu_3Se_2(s) \tag{6}$$

Besides, it is known that $CuSe_2$ melts incongruently to CuSe + Se around 340 °C and CuSe converts to $Cu_{2-x}Se$ above 350 °C [40]. This explains the absence of $CuSe_2$ or CuSe in the films obtained in the 350–400 °C range, because any other decomposition or sublimation is detected beyond 500 °C [40].

In order to compare the crystallinity of the various samples, mean crystallite sizes have been estimated from the main diffraction peak of each phase and they are represented in Fig. 4. For the hexagonal CuS phase detected in all the sulfurized films, the crystallite size is found in the range S(CuS) = 32–58 nm, increasing as the thickness and/or the heating temperature increase. The same behavior has been observed in copper sulfide layers prepared by dip coating [24], chemical bath deposition [25] or spray pyrolysis [41]. Otherwise, Cu_xS crystallite sizes below 6 nm have been synthesized by sol–gel [42] and solution-phase reaction [43, 44], near to the Bohr radius estimated for this material [18]. Superior sizes have been achieved for the hexagonal CuSe in the single-phase samples selenized at 250–300 °C, S(CuSe) = 74–83 nm, although its size decreases to S(CuSe) = 46–66 nm when additional $CuSe_2$ appears for the thickest layers, with $S(CuSe_2)$ = 58–60 nm. A

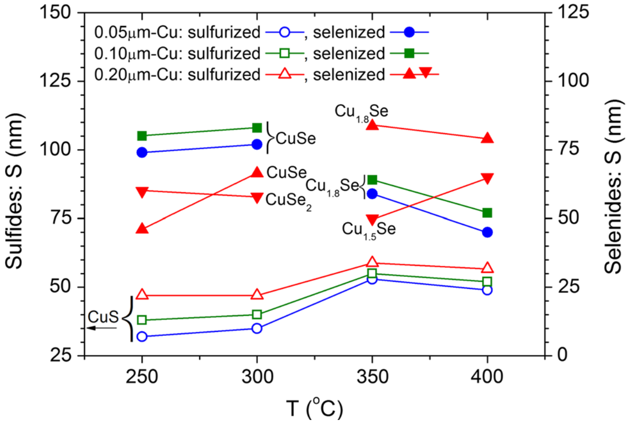

Figure 4 Evolution of the mean crystallite size for the various sulfide and selenide phases obtained as a function of the reaction temperature and Cu film thickness.

larger variation is detected for the cubic $Cu_{1.8}Se$ obtained at 350–400 °C, S($Cu_{1.8}Se$) = 45–83 nm, for which the crystallite size increases with the film thickness but it decreases when the heating temperature increases. This is attributed to some evolution from cubic $Cu_{1.8}Se$ to tetragonal $Cu_{1.5}Se$ at the highest selenization temperature, as it is evidenced in the thickest layers with S($Cu_{1.5}Se$) = 50–65 nm. These crystallite sizes are in the same order than reported for other Cu_xSe films obtained by chemical bath deposition [26] or screen printing [5].

AFM analysis performed on the layer surface has shown that root-mean-square roughness (R_q) increases when the mean crystallite size increases. Such correlation between morphology and crystallinity is illustrated in Fig. 5 for the thinnest single-phase samples synthesized at 250 and 350 °C. It should be noted that all the evaporated copper films had a very small roughness ($R_q = 5 \pm 1$ nm). The smoothest surface ($R_q = 15$ nm) corresponds to CuS obtained at 250 °C with the smallest crystallites ($S = 32$ nm), and the increment in the sulfurization temperature makes to increase both the crystallite size ($S = 53$ nm) and the roughness ($R_q = 80$ nm). Otherwise, CuSe obtained at 250 °C displays a rougher surface ($R_q = 175$ nm) in accordance with its large crystallite size ($S = 74$ nm), and the rise in the selenization temperature produces phase transformation to $Cu_{1.8}Se$ with lower crystallinity ($S = 59$ nm) and roughness ($R_q = 140$ nm). Similar values have been reported for other Cu_xS and Cu_xSe thin films [41, 45, 46], although a clear correlation between the crystallite size and the surface roughness cannot be established when they are small variations in crystallinity or coexistence of different phases.

The influence of the heating temperature on the optical characteristics is represented in Fig. 6. Overall, the transmittance spectrum shows a maximum located in the range $\lambda = 600$–800 nm, where the reflectance has a minimum and then increases mostly in the infrared, being the maximum reflectance values higher for the sulfide samples. For a same heating temperature, the transmittance maximum and reflectance minimum are located at a higher wavelength for the selenide than the sulfide film, but in both cases they move toward near infrared when the temperature increases. The optical absorption coefficients (α), calculated from T and R spectra, have evidenced two different absorption phenomena that are acting simultaneously in these layers and determine the position of the maximum and minimum observed.

All the samples exhibit a great α increment in the ultraviolet region, where the absorption is dominated by the bandgap of the semiconductor. The experimental data in Fig. 7 show a good fit to the expression for direct allowed interband transitions [47]: $\alpha^2 = (A/E)^2(E - E_g)$, where A is a constant related to the transition probability, E the radiation energy, and E_g the bandgap energy. Such gap energy is found higher for the sulfide layers, $E_g = 1.74$–2.22 eV, than for the selenide films, $E_g = 0.80$–1.37 eV, including in these ranges the various thicknesses and reaction temperatures. The smallest gap values correspond to the thickest films prepared at the lowest temperature, which have the lowest copper-to-chalcogen atomic ratio. Some band gap widening due to quantum confinement has been reported for copper chalcogenide nanocrystals with sizes below 6 nm [18, 42, 44], but this effect is discarded here owing to the large crystallite sizes obtained for the various phases.

The samples show also an absorption peak in the near infrared that is due to plasmon resonance, the collective oscillation of free carriers in response to the radiation, where α is connected to the hole density and mobility (N_p and μ_p) through the plasmon and damping energies (E_p and E_Γ) [48, 49]:

$$\alpha^2(E) \propto \frac{E_\Gamma}{(E - E_p)^2 + E_\Gamma^2} \quad (7)$$

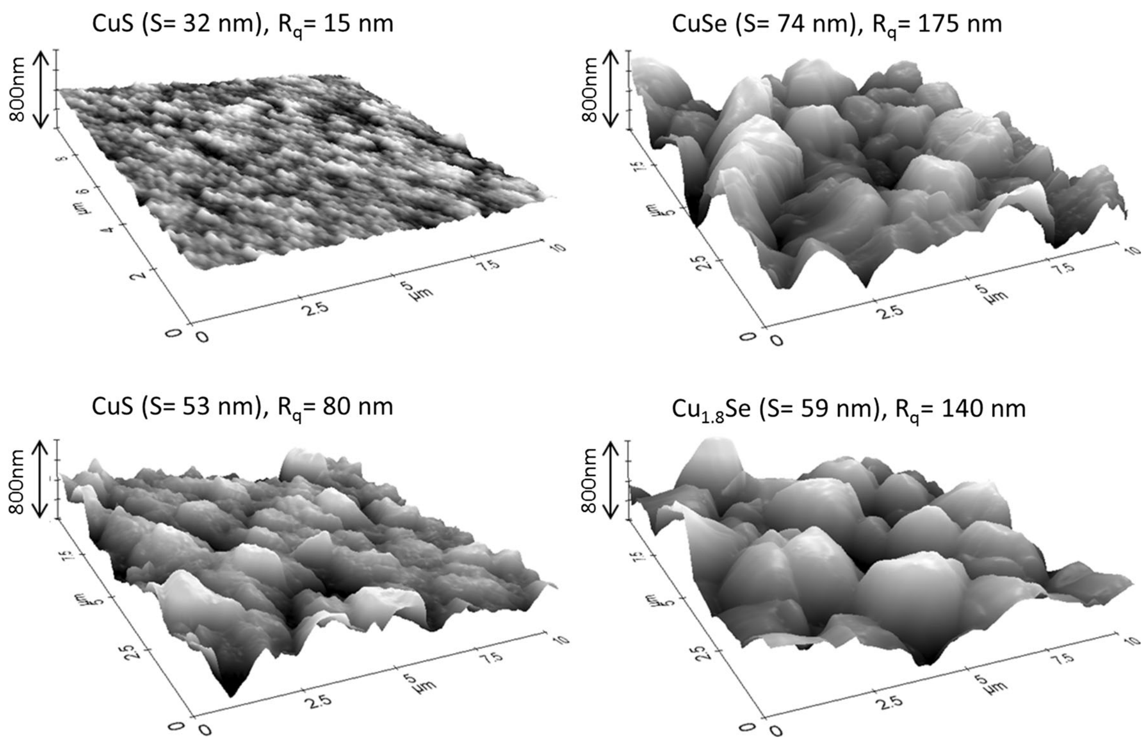

Figure 5 AFM images corresponding to the thinnest Cu films sulfurized or selenized at 250 °C (*up*) and 350 °C (*down*). The respective crystallite size (S) and root-mean-square roughness (R_q) are included for comparison.

$$\mu_p = \frac{\hbar q}{m^* E_\Gamma} \tag{8}$$

$$N_p = \frac{m^* \varepsilon_\infty \varepsilon_0}{\hbar^2 q^2}\left(E_p^2 + E_\Gamma^2\right) \tag{9}$$

Here ε_∞ and ε_0 are the relative high frequency and the vacuum permittivities, m^* is the conductivity effective mass, q is the carriers charge, and $\hbar$ is the reduced Planck constant. The plasmonic characteristics (E_p and E_Γ) have been obtained by fitting the infrared optical data to Eq. (7), as it is illustrated in Fig. 7, whereas the carrier density and mobility have been acquired independently by Hall effect measurements (N_H and μ_H). Then, the effective mass has been calculated from Eq. (8) by substitution of the respective E_Γ and Hall mobility values (assuming $\mu_p = \mu_H$). In this way, a low effective mass for holes ($m^* \sim 0.8\ m_e$) has been found in the present sulfide and selenide layers, according to previous reports for these materials [12, 44, 50]. Subsequently, the carrier density N_p has been estimated from Eq. (9) with the optical data and taking $\varepsilon_\infty = 10$, as stated for other copper chalcogenide nanocrystals [21, 44, 51], which has given a good concordance between the N_p and N_H values obtained for the various samples. It should be noted that some of the thinnest copper selenide films gave no electrical conductivity in the Hall effect measurements. This is attributed to the high roughness-to-thickness ratio for those layers, which hinders the continuity of the electrical current along the whole sample area.

The combination of optical and compositional data has revealed some interesting relations that are illustrated in Fig. 8, where the carrier concentration and the gap energy are plotted as a function of the copper-to-chalcogen atomic ratio (x = Cu/S or Cu/Se). For both sulfide and selenide layers, the carrier density decreases when the copper ratio increases according to the expression $N_p = 8 \times 10^{21} + 10^{24}\, e^{-6x}\,(\mathrm{cm}^{-3})$. Otherwise, the gap energy increases when the copper proportion increases, with a same tendency but different superior limit for the copper sulfide layers: $E_g = 2.4 - 2\,e^{-2x}\,(\mathrm{eV})$, and the copper selenides films: $E_g = 1.4 - 2\,e^{-2x}\,(\mathrm{eV})$. The highest gap values achieved at relatively high Cu ratios are within the widest reported for these nanocrystalline materials, that is 2.4 eV for copper sulfides [52–54] and 1.4 eV for copper selenides [55–57]. Then, the progressive creation of copper vacancies (when the x value decreases) makes to increase the carrier

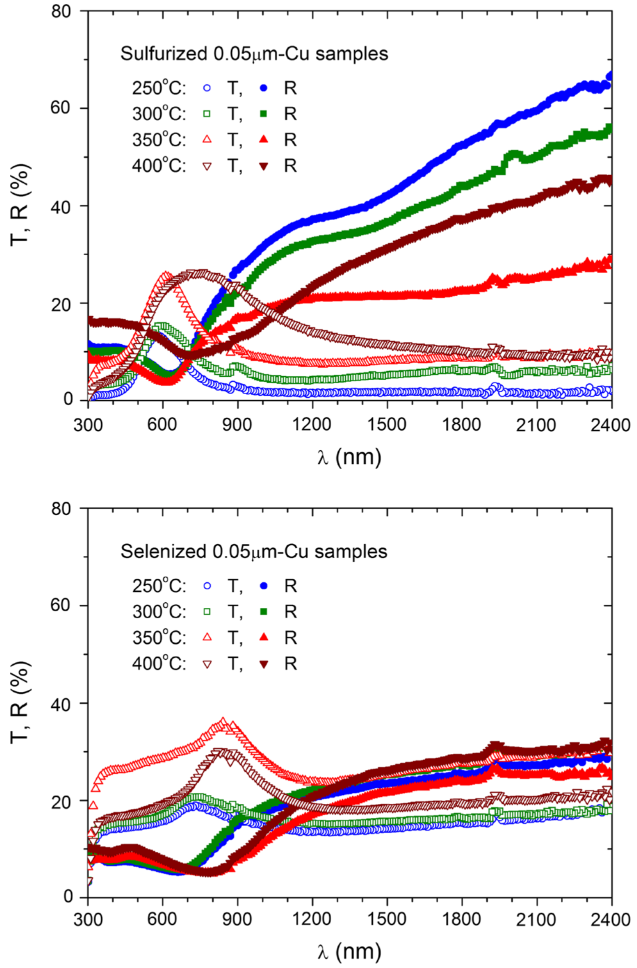

Figure 6 Optical transmittance and reflectance spectra as a function of the radiation wavelength for the thinnest Cu films after sulfurization or selenization at different temperatures.

concentration and narrow the bandgap, following the relationship $\Delta E_g = -2 \times 10^{-8}(\Delta N_p)^{1/3}$ that has been already stated in different p-type semiconductors [17].

In other cases, some increase in the carrier concentration due to copper vacancies formation is accompanied by the increment in both E_p and E_g energies, being $E_p \propto N_p^{1/2}$ according to Eq. (9) and the gap broadening attributed to the Burstein–Moss effect when the Fermi energy level decreases below the highest valence band states [16, 44], for which a dependence in the form $\Delta E_g^{BM} \propto N_p^{2/3}$ is expected [16]. Nevertheless, for greater carrier densities a sudden decrease in the optical gap can prevail due to semiconductor–metal transition [58]. This produces a bandgap narrowing that can be estimated by using

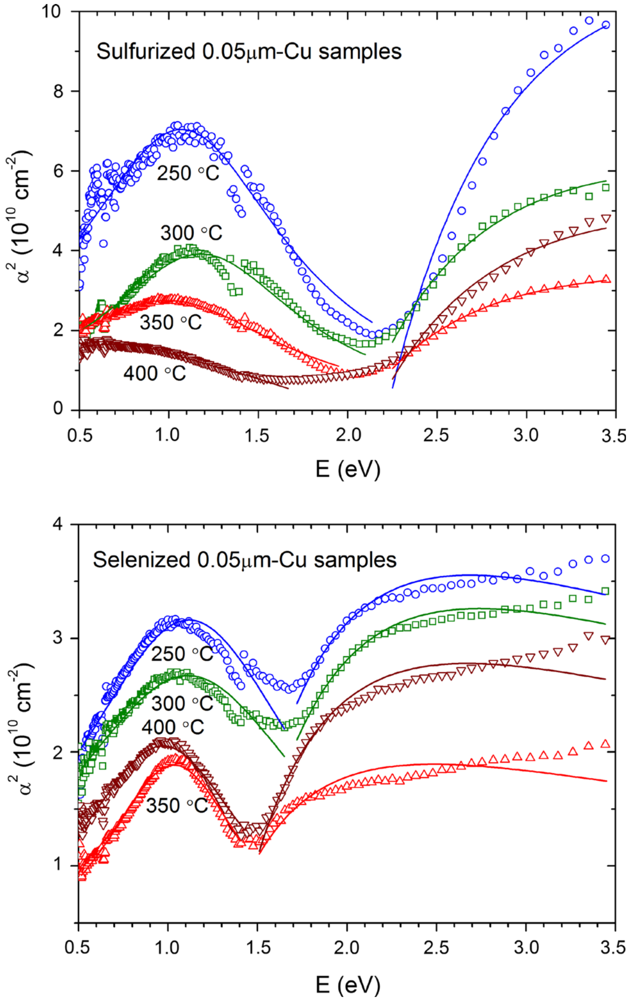

Figure 7 Optical absorption coefficient as a function of the radiation energy for the same samples represented in Fig. 6.

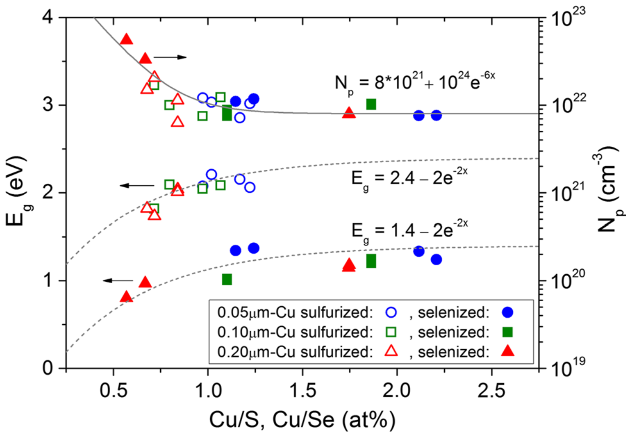

Figure 8 Evolution of the gap energy and carrier concentration as a function of the composition (x = Cu/S or Cu/Se atomic ratio) for the samples with various thicknesses and reaction temperatures.

the weakly interacting electron gas model [59]: $\Delta E_g^{GM} = -\frac{q^2}{2\pi\varepsilon\varepsilon_0}\left(\frac{3}{\pi}N_p\right)^{1/3}$, expression that represents properly the experimental data for the present samples with a metallic character, being here $\Delta E_g = \Delta E_g^{GM}$.

The electrical characteristics determined by Hall effect measurements are shown in Fig. 9. It shows that hole mobility increases with the carrier concentration in the form $\mu \propto N^{1/2}$, and the conductivity increases also accordingly $\sigma = qN\mu \propto N^{3/2}$. In general, for highly doped semiconductors the electrical transport is dominated by optical phonon scattering and ionized impurity scattering, which depend on the temperature and the carrier concentration in opposite ways [60]. Lattice ions, which are needed to balance the free carriers charge, make to decrease notably the mobility with increasing carrier density [61]. However, for copper chalcogenides and other materials with a high ε_∞, the lattice ions are effectively screened from the free carriers [62], and the ionized impurity scattering is less relevant. Otherwise, phonon scattering tends to decrease at high carrier densities, and thus, it makes to increase the mobility when the carrier concentration increases [63]. This last tendency is observed for the present samples, which is according to their metallic character. Similar metallic behavior, with phonon scattering dominating the electrical conductivity at room temperature, has been reported for analogous copper chalcogenide layers with hole concentrations around 10^{22} cm^{-3} [14, 15].

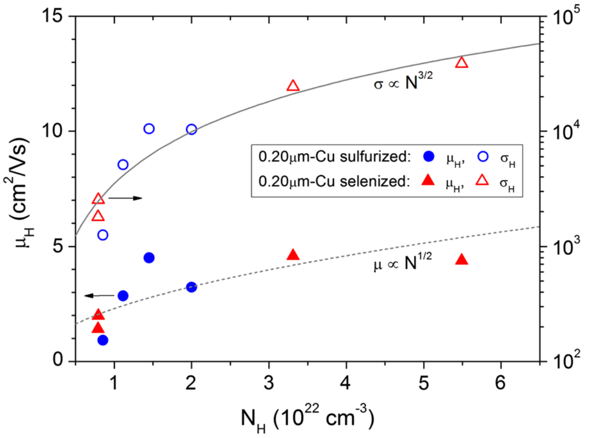

Figure 9 Evolution of the Hall mobility and conductivity as a function of the carrier concentration for the thickest Cu films after sulfurization or selenization at different temperatures.

Conclusions

Cu_xS and Cu_xSe nanocrystalline layers have been obtained by reaction of evaporated Cu (0.05–0.20 μm thicknesses) with elemental sulfur or selenium at temperatures ranging from 250 to 400 °C. The copper-to-chalcogen atomic ratio is found increasing when the heating temperature increases and/or the film thickness decreases, in a wider interval for copper selenides ($x = 0.6$–2.2) than copper sulfides ($x = 0.7$–1.2), which is related to a higher thermal stability of the sulfide compounds.

All the sulfurized films crystallized in the hexagonal CuS phase, with mean crystallite size increasing from 32 to 58 nm when the layer thickness and the heating temperature increase, although some additional cubic $Cu_{1.8}S$ appears after heating at 400 °C. Similarly, the samples selenized at 250–300 °C have shown crystallization of hexagonal CuSe, together with orthorhombic $CuSe_2$ for the layers with the lowest Cu/Se $\sim$ 0.6, but at 350–400 °C it is replaced by cubic $Cu_{1.8}Se$, with some tetragonal Cu_3Se_2 for the films with Cu/Se < 1.8. Copper selenide phases achieved higher crystallites sizes than the analogous copper sulfide.

Thus, thermal annealing involves phase transitions that increase the crystal symmetry from hexagonal to cubic and tetragonal structures, making to decrease the copper-to-chalcogen ratio in the way. Besides, the surface roughness is found related to the crystallinity, with root-mean-square roughness increasing from $R_q = 15$ to 80 nm when the CuS crystallite size increases from 32 to 53 nm, and higher to $R_q = 175$ nm for the CuSe crystallites with 74 nm or $R_q = 140$ nm for the $Cu_{1.8}Se$ crystallites with 59 nm mean sizes.

Both sulfide and selenide layers evidenced plasmonic characteristics in the near infrared, which are according to a low effective mass for holes ($m^* \sim 0.8\, m_e$) and high carrier densities around 10^{22} cm^{-3}. The progressive creation of copper vacancies (when the x value decreases) makes to increase the carrier concentration as $N_p = 8 \times 10^{21} + 10^{24}\, e^{-6x}(\text{cm}^{-3})$ and narrow the bandgap for the copper sulfide layers: $E_g = 2.4 - 2e^{-2x}(\text{eV})$, and for the copper selenides films: $E_g = 1.4 - 2e^{-2x}(eV)$. The general relationship established, $\Delta E_g = -2 \times 10^{-8} (\Delta N_p)^{1/3}$, is properly represented by a weakly interacting electron gas model. Moreover, the increment in the hole mobility with the carrier concentration, $\mu \propto N^{1/2}$, confirms the metallic character of the samples, with electrical transport dominated by phonon scattering.

Acknowledgements

This work has been supported by the Spanish Ministry of Economy, Industry and Competitiveness through the MAT2015-66649-R project and the CIEMAT Photovoltaic Program.

References

[1] Kundu J, Pradhan D (2014) Controlled synthesis and catalytic activity of copper sulfide nanostructured assemblies with different morphologies. ACS Appl Mater Interfaces 6:1823–1834. doi:10.1021/am404829g

[2] Sagade AA, Sharma R (2008) Copper sulphide (Cu_xS) as an ammonia gas sensor working at room temperature. Sens Actuators B Chem 133:135–143. doi:10.1016/j.snb.2008.02.015

[3] Chen YH, Davoisne C, Tarascon JM, Guery C (2012) Growth of single-crystal copper sulfide thin films via electrodeposition in ionic liquid media for lithium ion batteries. J Mater Chem 22:5295–5299. doi:10.1039/C2jm16692e

[4] Aguilar JO, Gomez-Daza O, Brito LA et al (2005) Optical and mechanical characteristics of clear and solar control laminated glass using zinc sulphide and copper sulphide thin films. Surf Coat Technol 200:2557–2565. doi:10.1016/j.surfcoat.2004.10.140

[5] Zhang H, Wang C, Peng W et al (2016) Quantum dot sensitized solar cells with efficiency up to 8.7% based on heavily copper-deficient copper selenide counter electrode. Nano Energy 23:60–69. doi:10.1016/j.nanoen.2016.03.009

[6] Korala L, McGoffin JT, Prieto AL (2016) Enhanced conductivity in CZTS/$Cu_{2-x}Se$ nanocrystal thin films: growth of a conductive shell. ACS Appl Mater Interfaces 8:4911–4917. doi:10.1021/acsami.5b11037

[7] Blachnik R, Müller A (2000) The formation of Cu_2S from the elements: I. Copper used in form of powders. Thermochim Acta 361:31–52

[8] Glazov VM, Pashinkin AS, Fedorov VA (2000) Phase equilibria in the Cu–Se system. Inorg Mater 36:641–652. doi:10.1007/BF02758413

[9] Zhang Y, Wang Y, Xi L et al (2014) Electronic structure of antifluorite Cu_2X (X = S, Se, Te) within the modified Becke–Johnson potential plus an on-site Coulomb U. J Chem Phys. doi:10.1063/1.4865257

[10] Choi JH, Han YK (2015) Structural, electronic, and optical properties of bulk Cu_2Se. Curr Appl Phys 15:1417–1420. doi:10.1016/j.cap.2015.08.006

[11] Liu G, Schulmeyer T, Brötz J et al (2003) Interface properties and band alignment of Cu_2S/CdS thin film solar cells. Thin Solid Films 431–432:477–482. doi:10.1016/S0040-6090(03)00190-1

[12] Lukashev P, Lambrecht WRL, Kotani T, van Schilfgaarde M (2007) Electronic and crystal structure of $Cu_{2-x}S$: full-potential electronic structure calculations. Phys Rev B 76:195202. doi:10.1103/PhysRevB.76.195202

[13] Coughlan C, Ibáñez M, Dobrozhan O et al (2017) Compound copper chalcogenide nanocrystals. Chem Rev. doi:10.1021/acs.chemrev.6b00376

[14] He Y, Polity A, Österreicher I (2001) Hall effect and surface characterization of Cu_2S and CuS films deposited by RF reactive sputtering. Phys B Condens Matter 310:1069–1073

[15] Wang L, Ren B, Weng L et al (2015) Metal-semiconductor transition in CuS–$Cu_{1.8}S$ mixed phase thin films. Vacuum 112:70–72. doi:10.1016/j.vacuum.2014.11.018

[16] Comin A, Manna L (2014) New materials for tunable plasmonic colloidal nanocrystals. Chem Soc Rev 43:3957–3975. doi:10.1039/c3cs60265f

[17] Jain SC, McGregor JM, Roulston DJ (1990) Band-gap narrowing in novel III–V semiconductors. J Appl Phys 88:3747–3749

[18] Zhao Y, Pan H, Lou Y et al (2009) Plasmonic $Cu_{2-x}S$ nanocrystals: optical and structural properties of copper-deficient copper(I) sulfides. J Am Chem Soc 131:4253–4261. doi:10.1021/ja805655b

[19] Dorfs D, Härtling T, Miszta K et al (2011) Reversible tunability of the NIR valence band plasmon resonance in $Cu_{2-x}Se$ nanocrystals. J Am Chem Soc 133:11175–11180. doi:10.1021/ja2016284

[20] Kriegel I, Jiang C, Rodríguez-Fernández J et al (2012) Tuning the excitonic and plasmonic properties of copper chalcogenide nanocrystals. J Am Chem Soc 134:1583–1590. doi:10.1021/ja207798q

[21] Xie Y, Carbone L, Nobile C et al (2013) Metallic-like stoichiometric copper sulfide nanocrystals: phase- and shape-selective synthesis, near-infrared surface plasmon resonance properties, and their modeling. ACS Nano 7:7352–7369. doi:10.1021/nn403035s

[22] West PR, Ishii S, Naik GV et al (2010) Searching for better plasmonic materials. Laser Photonics Rev 4:795–808. doi:10.1002/lpor.200900055

[23] Teranishi T, Eguchi M, Kanehara M, Gwo S (2011) Controlled localized surface plasmon resonance wavelength for conductive nanoparticles over the ultraviolet to near-infrared region. J Mater Chem 21:10238. doi:10.1039/c0jm04545d

[24] Rafea MA, Farag AAM, Roushdy N (2012) Controlling the crystallite size and influence of the film thickness on the optical and electrical characteristics of nanocrystalline Cu_2S films. Mater Res Bull 47:257–266. doi:10.1016/j.materresbull.2011.11.035

[25] Dhondge AD, Gosavi SR, Gosavi NM (2015) Influence of thickness on the photosensing properties of chemically synthesized copper sulfide thin films. World J Condens Matter Phys 5:1–9

[26] Dhanam M, Manoj PK, Prabhu RR (2005) High-temperature conductivity in chemical bath deposited copper selenide thin films. J Cryst Growth 280:425–435. doi:10.1016/j.jcrysgro.2005.01.111

[27] Franzen S (2008) Surface plasmon polaritons and screened plasma absorption in indium tin oxide compared to silver and gold. J Phys Chem C 112:6027–6032. doi:10.1021/jp7097813

[28] Losego MD, Efremenko AY, Rhodes CL et al (2009) Conductive oxide thin films: model systems for understanding and controlling surface plasmon resonance. J Appl Phys 106:24903. doi:10.1063/1.3174440

[29] Zang Z, Nakamura A, Temmyo J (2013) Single cuprous oxide films synthesized by radical oxidation at low temperature for PV application. Opt Express 21:11448. doi:10.1364/OE.21.011448

[30] Zang Z, Nakamura A, Temmyo J (2013) Nitrogen doping in cuprous oxide films synthesized by radical oxidation at low temperature. Mater Lett 92:188–191. doi:10.1016/j.matlet.2012.10.083

[31] Caballero R, Guillén C, Gutiérrez MT, Kaufmann CA (2006) $CuIn_{1-x}Ga_xSe_2$-based thin-film solar cells by the selenization of sequentially evaporated metallic layers. Prog Photovolt Res Appl 14:145–153

[32] López-García J, Placidi M, Fontané X et al (2015) $CuIn_{1-x}Al_xSe_2$ thin film solar cells with depth gradient composition prepared by selenization of evaporated metallic precursors. Sol Energy Mater Sol Cells 132:245–251. doi:10.1016/j.solmat.2014.09.003

[33] López-García J, Guillén C (2009) Adjustment of the selenium amount provided during formation of $CuInSe_2$ thin films from the metallic precursors. Phys Status Solidi Appl Mater Sci 206:84–90

[34] Xue MZ, Zhou YN, Zhang B et al (2006) Fabrication and electrochemical characterization of copper selenide thin films by pulsed laser deposition. J Electrochem Soc 153:A2262–A2268. doi:10.1149/1.2358854

[35] Liu L, Liu C, Fu W et al (2016) Phase transformations of copper sulfide nanocrystals: towards highly efficient quantum-dot-sensitized solar cells. ChemPhysChem 17:771–776. doi:10.1002/cphc.201500627

[36] Selivanov EN, Gulyaeva RI, Vershinin AD (2007) Thermal expansion and phase transformations of copper sulfides. Inorg Mater 43:573–578. doi:10.1134/S0020168507060027

[37] Skomorokhov AN, Trots DM, Knapp M et al (2006) Structural behaviour of beta-$Cu_{2-x}Se$ ($x = 0, 0.15, 0.25$) in dependence on temperature studied by synchrotron powder diffraction. J Alloys Compd 421:64–71. doi:10.1016/j.jallcom.2005.10.079

[38] Jackson AJ, Tiana D, Walsh A (2016) A universal chemical potential for sulfur vapours. Chem Sci 7:1082–1092. doi:10.1039/C5SC03088A

[39] Olin A, Noläng B, Osadchii EG et al (2005) Chemical thermodynamics of selenium. Elsevier, Amsterdam

[40] Gobeaut A, Laffont L, Tarascon JM et al (2009) Influence of secondary phases during annealing on re-crystallization of $CuInSe_2$ electrodeposited films. Thin Solid Films 517:4436–4442. doi:10.1016/j.tsf.2009.01.043

[41] Cuevas A, Romero R, Leinen D et al (2015) Effect of the stoichiometry of Cu_xS thin films on the optical and electrical properties and the solar thermal performance. Sol Energy Mater Sol Cells 134:199–208. doi:10.1016/j.solmat.2014.11.048

[42] Li J, Jiu TG, Tao GH et al (2014) Manipulating surface ligands of copper sulfide nanocrystals: synthesis, characterization, and application to organic solar cells. J Colloid Interface Sci 419:142–147. doi:10.1016/j.jcis.2013.12.057

[43] Wu Y, Wadia C, Ma W et al (2008) Synthesis and photovoltaic application of copper(I) sulfide nanocrystals. Nano Lett 8:2551–2555. doi:10.1021/nl801817d

[44] Luther JM, Jain PK, Ewers T, Alivisatos AP (2011) Localized surface plasmon resonances arising from free carriers in doped quantum dots. Nat Mater 10:361–366. doi:10.1038/nmat3004

[45] Isac L, Popovici I, Enesca A, Duta A (2010) Copper sulfide (Cu_xS) thin films as possible p-type absorbers in 3D solar cells. Energy Proc 2:71–78. doi:10.1016/j.egypro.2010.07.013

[46] Sharma R, Sagade AA, Gosavi SR et al (2009) Effect of high electronic energy loss of 100 MeV gold heavy ions in copper chalcogenides (CuX, X = S, Se) at nanoscale: opto-electronic properties study. J Non Cryst Solids 355:1653–1658. doi:10.1016/j.jnoncrysol.2009.05.055

[47] Viezbicke BD, Patel S, Davis BE, Birnie DP (2015) Evaluation of the Tauc method for optical absorption edge determination: ZnO thin films as a model system. Phys Status Solidi 252:1700–1710. doi:10.1002/pssb.201552007

[48] Barnabe A, Thimont Y, Lalanne M et al (2015) P-type conducting transparent characteristics of delafossite Mg-doped $CuCrO_2$ thin films prepared by RF-sputtering. J Mater Chem C 3:6012–6024. doi:10.1039/C5TC01070E

[49] Guillén C, Herrero J (2016) Structural and plasmonic characteristics of sputtered SnO_2: Sb and ZnO: Al thin films as a function of their thickness. J Mater Sci 51:7276–7285. doi:10.1007/s10853-016-0010-9

[50] Hsu SW, Ngo C, Tao AR (2014) Tunable and directional plasmonic coupling within semiconductor nanodisk assemblies. Nano Lett 14:2372–2380. doi:10.1021/nl404777h

[51] Liu M, Xue X, Ghosh C et al (2015) Room-temperature synthesis of covellite nanoplatelets with broadly tunable localized surface plasmon resonance. Chem Mater 27:2584–2590. doi:10.1021/acs.chemmater.5b00270

[52] Quintana-Ramirez PV, Arenas-Arrocena MC, Santos-Cruz J et al (2014) Growth evolution and phase transition from chalcocite to digenite in nanocrystalline copper sulfide: morphological, optical and electrical properties. Beilstein J Nanotechnol 5:1542–1552. doi:10.3762/bjnano.5.166

[53] Grozdanov I, Najdoski M (1995) Optical and electrical properties of copper sulfide films of variable composition. J Solid State Chem 114:469–475. doi:10.1006/jssc.1995.1070

[54] Rodríguez-Lazcano Y, Martínez H, Calixto-Rodríguez M, Núñez Rodríguez A (2009) Properties of CuS thin films treated in air plasma. Thin Solid Films 517:5951–5955. doi:10.1016/j.tsf.2009.03.075

[55] Haram SK, Santhanam KSV (1994) Electroless deposition of orthorhombic copper (I) selenide and its room temperature phase transformation to cubic structure. Thin Solid Films 238:21–26. doi:10.1016/0040-6090(94)90642-4

[56] Hu Y, Afzaal M, Malik MA, O’Brien P (2006) Deposition of copper selenide thin films and nanoparticles. J Cryst Growth 297:61–65. doi:10.1016/j.jcrysgro.2006.08.038

[57] Bhuvaneswari PV, Ramamurthi K, Ramesh Babu R, Moorthy Babu S (2015) Structural, morphological, optical and electrical properties of $Cu_{0.87}Se$ thin films coated by electron beam evaporation method. Appl Phys A 120:1113–1120. doi:10.1007/s00339-015-9286-x

[58] Lu JG, Fujita S, Kawaharamura T et al (2007) Carrier concentration dependence of band gap shift in n-type ZnO: Al films. J Appl Phys 101:83705. doi:10.1063/1.2721374

[59] Kim WM, Kim JS, Jeong JH et al (2013) Analysis of optical band-gap shift in impurity doped ZnO thin films by using nonparabolic conduction band parameters. Thin Solid Films 531:430–435. doi:10.1016/j.tsf.2013.01.078

[60] Kasap S, Koughia C, Ruda H, Johanson R (2006) Electrical conduction in metals and semiconductors. In: Kasap S (ed) Springer handbook of electronic and photonic materials. Springer, Boston, pp 19–45

[61] Ellmer K (2001) Resistivity of polycrystalline zinc oxide films: current status and physical limit. J Phys D Appl Phys 34:3097–3108. doi:10.1088/0022-3727/34/21/301

[62] Mendelsberg RJ, Garcia G, Li H et al (2012) Understanding the plasmon resonance in ensembles of degenerately doped semiconductor nanocrystals. J Phys Chem C 116:12226–12231. doi:10.1021/jp302732s

[63] Ruda HE (1991) Compensation and transport characteristics of n-ZnTe. J Phys D Appl Phys 24:1158–1162. doi:10.1088/0022-3727/24/7/021